

Article

Experimental Investigation of Temperature Distribution in a Laminar Boundary Layer over a Heated Flat Plate with Localized Transverse Cold Air Injections

Muhammad Ehtisham Siddiqui ^{1,*}, Ammar A. Melaibari ^{1,†} and Fahad Sarfraz Butt ^{2,†}

¹ Mechanical Engineering Department, King Abdulaziz University, Jeddah 21589, Saudi Arabia; aamelaibari@kau.edu.sa

² Mechanical Engineering Department, HITEC University, Taxila 47080, Pakistan; fahadsarfrazbutt@gmail.com

* Correspondence: mesiddiqui@kau.edu.sa; Tel.: +96-655-218-4681

† These authors contributed equally to this work.

Abstract: This study presents an experimental investigation focused on the interaction between a transverse injection of cold air (blowing) and the boundary layer over a heated flat plate. The flat plate was equipped with a cylindrical coil heater positioned at its center along the flow direction. The constant heat flux was maintained using a variable resistance potentiometer. The flat plate with the heater was mounted inside a subsonic wind tunnel to sustain a constant laminar air flow. The primary objective of this research was to examine the effects of cold air injections through localized holes in the flat plate near the trailing edge on the thermal boundary layer thickness $\delta_t(x, Re_x, Pr)$. The thermal boundary layer thickness was measured using K-type thermocouples and PT-100 RTD sensors, which are made to move precise, small distances using a specially constructed traversing mechanism. Cold air was injected using purposefully fabricated metal capillary tubes force-fitted into holes through the hot flat plate. The metal tubes were thermally insulated using class-F insulation, which is used in electric motor windings. The presented work focused on a fixed free-stream velocity and a fixed cold-injection velocity less than the free-stream velocity but for two-variable heat fluxes. The results show that the thermal boundary layer thickness generally increased due to the secondary cold flow.

Keywords: heat transfer; boundary layer; laminar flow; heated flat plate; thermal boundary layer thickness; Rayleigh number; Reynolds number; transverse blowing; cold injection; transpired boundary layer



Citation: Siddiqui, M.E.; Melaibari, A.A.; Butt, F.S. Experimental Investigation of Temperature Distribution in a Laminar Boundary Layer over a Heated Flat Plate with Localized Transverse Cold Air Injections. *Energies* **2023**, *16*, 6171. <https://doi.org/10.3390/en16176171>

Academic Editors: Frede Blaabjerg and Dmitry Eskin

Received: 27 June 2023

Revised: 9 August 2023

Accepted: 18 August 2023

Published: 25 August 2023



Copyright: © 2023 by the authors. Licensee MDPI, Basel, Switzerland. This article is an open access article distributed under the terms and conditions of the Creative Commons Attribution (CC BY) license (<https://creativecommons.org/licenses/by/4.0/>).

1. Introduction

Boundary layers are thin, viscous-dominated regions adjacent to boundaries [1]. Hydrodynamic and thermal gradients generally only prevail inside the boundary layers; hence, these layers have been the subject of great interest for many decades. The drag on immersed bodies owes a lot to the boundary layers. The thicker the hydrodynamic boundary layer, the higher the friction drag on the immersed bodies [2], and the thicker the thermal boundary layer, the lower the heat transfer rate inside the boundary layer, especially from the surface to the boundary layer [3]. This study focuses on the laminar thermal boundary layers, which are amenable to analytical solutions; one iconic solution of such a type is the Blasius solution, which is only valid for laminar boundary layers [4]. The spread of the viscous region around an immersed body is dependent on various factors, which can be grouped into two non-dimensional numbers known as the Reynolds number $Re = \frac{U_\infty x}{\nu}$ and the Prandtl number $Pr = \frac{\nu}{\alpha}$, where $\nu(T)$ in m^2/s is the kinematic viscosity, x is the distance from the leading edge of the immersed body, U_∞ is the free-stream velocity and $\alpha(T)$ is the thermal diffusivity in m^2/s . Hence, thermal boundary layer thickness

can be expressed as $\delta_t(x, Re_x, Pr)$, where both non-dimensional numbers are temperature dependent [5].

The presence of transpiration within boundary layers on solid surfaces has attracted significant interest in various technical applications. In this context, "transpiration" encompasses both suction, where the flow direction normal to the surface is inward, and blowing, where the flow is directed outward from the surface [6]. Transpiration has been extensively studied as a means to enhance surface cooling or achieve drag reduction (blowing), control boundary layer separation and delay laminar-to-turbulent transition (suction) in aeronautical applications [7]. This approach finds application in cooling surfaces subjected to high heat fluxes, such as rocket engine combustion chambers, solar thermal collectors and turbines [8]. Injecting fluid through the surface assists in preventing surface overheating and melting.

Transpired boundary layers have the potential to reduce the drag experienced by objects moving through a fluid [9]. By introducing fluid through the surface, the flow around the object can be smoothed, leading to drag reduction. Additionally, transpired boundary layers offer the ability to control the flow separation of objects in a fluid medium [10]. Injecting fluid through the surface helps prevent flow separation, thereby enhancing the object's performance. Another advantage of transpired boundary layers is their ability to enhance mass transfer across a surface [11]. By injecting fluid through the surface, the diffusion rate of the fluid across the surface can be increased, making it beneficial for applications such as gas separation and chemical synthesis.

The insights gained from this research can aid in designing more efficient cooling mechanisms for power plants and electronic equipment, leading to enhanced energy efficiency and reduced environmental impact. Overall, this research has the potential to modernize multiple engineering domains, paving the way for more sustainable and innovative solutions in the face of evolving technological challenges.

Laminar transpired boundary layers were the focus of extensive investigation in the 1950s and 1960s. Authors of studies such as [11,12] in the 1950s and [10,13–16] in the 1960s performed notable research on wall heat transfer rates, employing analytical and approximate methods to address transpired boundary layers using a myriad of thermodynamic and hydrodynamic variables. The primary focus was on the exact solutions, which represented the order of the day, and on the physics of the processes, which was motivated primarily by the aeronautical technological advancements of that era. These analytical and approximate techniques were seldom complimented with experimental work, like in the case of Mickley [11], which directly relates to the studies performed in our proposed research work. It was reported in [11] that blowing increased the boundary layer thickness and hastened the laminar-to-turbulent transition, whereas suction delayed the transition and decreased the boundary layer thickness.

The height of supersonic and hypersonic interests the 1970s and 1980s significantly shifted the focus from laminar to turbulent boundary layers with and without transpiration. Ever since then, extensive efforts have been made to develop approximate methods to understand the complex mechanism inside transpired turbulent boundary layers, targeting the applications and purposes discussed in the opening paragraph. Notable works from these two decades on transpired laminar boundary layers are [17–20]. Similarly, the 1990s saw notable works on laminar transpired boundary layers [7,8,21].

More recently, in the last two decades, research works [22–27] have provided us with insights aiding our understanding of laminar transpired boundary layers, with new applications in renewable solar thermal energy systems. The study presented in this paper revisits classic, iconic works and tends to deviate from the stereotypical multifaceted and multivariate analysis by oversimplifying the form of temperature distribution inside thermal boundary layers to ascertain thermal thickness. This work may serve as a qualitative discussion of heat transfer inside thermal boundary layers through the increase or decrease in thermal boundary layer thickness. Furthermore, transpiration (blowing: cold air injections) was limited to a few locations near the trailing edge only. Blowing velocity

was deliberately kept lower than the free-stream velocity in order to limit the disruptions to the free stream and to the boundary layer itself.

The research paper is organized into four coherent sections, namely the introduction, which provides an overview of the study's objectives and significance; the experimental setup and instrumentation, detailing the methods used to conduct the research; the results, presenting the findings from the temperature distribution analysis; and finally the discussion and conclusion, where the implications and significance of the results are critically evaluated, leading to a comprehensive conclusion.

2. Experimental Setup and Instrumentation

The experimental setup consists of a G.U.N.T subsonic wind tunnel (Figure 1a) with a transparent test section of specific dimensions (42.60 cm × 26.60 cm × 31.7 cm). Inside the test section, a sharp-edged mild steel flat plate with a thickness of 3 mm and a dimension of 54.10 cm × 25.40 cm is mounted on a platform table (Figure 1b). A two-degree-of-freedom, transverse and longitudinal, traversing mechanism is mounted on top of the wind tunnel's test section (Figure 1c). This mechanism is used to precisely position either the pitot-static probe or the temperature measurement instrumentation. A heating wire, rated for AC power of 1000 W, is wrapped around a cylindrical base with a diameter of 1 inch. This wire is positioned along the centerline below the 3 mm thick flat plate, and it is spaced 3 mm away from the plate using thin Teflon brackets (Figure 1d). The effective dimensions of the flat plate are 43.20 cm × 2.54 cm × 3 mm. The reduced effective width is due to the flow symmetry in the z-direction, and the reduced effective length is employed to avoid trailing edge temperature gradient effects. The effective length achieves uniform temperature (± 0.5 °C) along its entire spread.

Die-cast metal tubes (Figure 2a) with a thickness of half a millimeter and an outer diameter nearly the same as the holes in the plate are securely fitted without protruding through the plate's surface. To ensure thermal insulation, the metal tubes are encased in Class-F motor winding insulation.

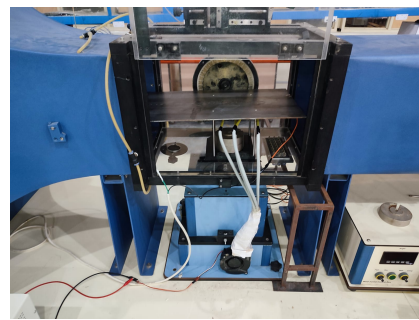
The instrumentation comprises various components. These include a Pitot-static probe used for measuring velocity within the test section. Additionally, there are two K-type thermocouples (one bulb-type and one needle-type), along with a PT-100 RTD needle-type sensor (as shown in Figure 2b,c). An amplifier module (shown in Figure 2d) and an Arduino Uno are utilized for data acquisition (visible in Figure 3a). An infrared thermometer heat gun is also present (Figure 3b). To regulate the heat flux of the heater, a potentiometer is incorporated (Figure 3c). Lastly, a variable RPM fan is connected to regulated DC power supply (Figure 3d).

The infrared thermometer heat gun is used exclusively to establish near-ambient conditions at the periphery of the test section and to quickly approximate the plate temperatures. It is important to note that the subsequent sections exclusively present readings derived from thermocouples and RTDs. The accuracies of the K-type thermocouples and RTD PT-100 sensors are 0.4% and 0.2% of the measured temperatures, respectively.

The velocities within the test section are determined using the digital differential pressure output displayed on an acquisition panel, obtained from a Pitot-static probe. As we observe in the upcoming sections, the highest Reynolds number in this research is approximately 10^3 , which is two orders of magnitude lower than the critical Reynolds number for early transition. This indicates that the flow field is predominantly laminar, eliminating the need for temporal averaging of the temperature and velocity fields, as typically required in the case of turbulent flows.



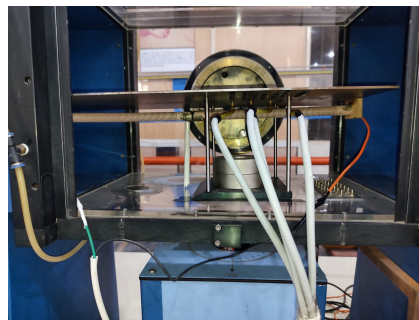
(a) Subsonic Wind Tunnel



(b) Test section



(c) Traversing mechanism

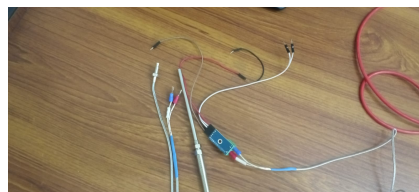


(d) Plate, heater and platform table

Figure 1. Experimental Setup.



(a) Metal tube and insulation



(b) Thermocouples



(c) PT100 RTD sensor



(d) Amplifier Module

Figure 2. Tubes and heat sensors.



(a) Arduino Uno



(b) Infrared thermometer heat gun

Figure 3. Cont.

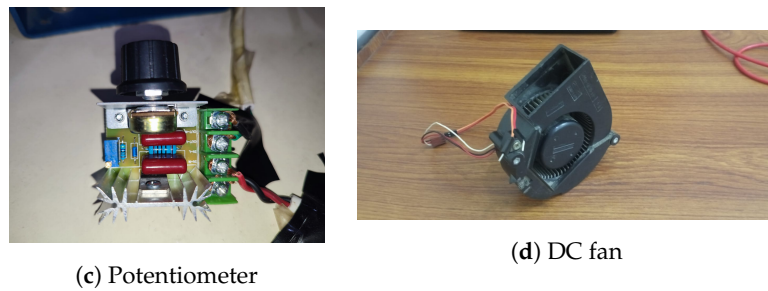


Figure 3. Data Acquisition and support equipment.

The flat plate features four 3.5 mm holes drilled into it, starting from the trailing edge and progressing towards the leading edge, covering a distance of 33.9 cm. The holes are spaced apart by 3.1 cm (Figure 4). This perforated flat plate is used in the second experimental study as outlined in Sections 3 and 3.2.



Figure 4. Plate Perforations (holes).

3. Results

This research consists of two distinct experimental studies. The first study is a validation analysis, primarily focused on measuring the thermal boundary layer thickness $\delta_t(x)$ along a heated flat plate without perforations or cold injections. The second study also measures $\delta_t(x)$ but with an addition of cold injections blowing through perforations, as shown in Figure 4.

3.1. Validation Study: Thermal Boundary Layer Thickness over a Regular Heated Flat Plate

The validation case study aims to verify the accuracy of the experimental setup, instrumentation and measurement techniques employed in this research work. This is accomplished by measuring the thermal boundary layer thickness $\delta_t(x)$ over heated flat plate and subsequently comparing these measurements with the analytical results by Blasius (1905), as mentioned in Introduction, Section 1.

The validation study comprises two distinct case studies, namely No-Inj-Tf50 and No-Inj-Tf42, as outlined in Table 1. These case studies are conducted at two different uniform plate temperatures, $T_p = 133.5\text{ }^\circ\text{C}$ and $T_p = 103.5\text{ }^\circ\text{C}$, respectively. It is important to note that these uniform equilibrium plate temperatures are achieved by applying a constant heat flux generated by the heater while ensuring the absence of any airflow ($U_\infty = 0\text{ m/s}$). The intensity of the heat flux is regulated by adjusting the resistance of the potentiometer,

and it requires approximately 45 min to achieve equilibrium conditions within the wind tunnel’s test section.

Table 1. Important parameters of the two validation case studies.

Case-Study	U_{∞} (m/s)	T_{∞} (°C)	T_p (°C)	T_{pw} (°C)	T_f (°C)	ν (m ² /s)	Pr
No-Inj-Tf50	0.5	29.38	133.5	71.5	50.44	1.95×10^{-5}	0.718
No-Inj-Tf42	0.5	30.09	103.5	55.5	42.79	1.92×10^{-5}	0.716

Temperatures have an uncertainty of ± 0.10 °C.

The plate temperature starts to drop as soon as the wind tunnel generates a wind speed of 0.5 m/s in the test section. It takes approximately 40 min to achieve thermal equilibrium and reach uniform plate temperatures (T_{pw}), as mentioned in Table 1. These T_{pw} are subsequently used to estimate film temperatures, which are then employed in estimating various thermophysical properties of the air.

The thermal boundary layer thickness, denoted as $\delta(x)$, is measured at four distinct locations along the centerline, starting from the trailing edge and moving towards the leading edge. These locations are specified in Table 2. The experimental setup and instrumentation details can be found in Section 2. The selection of locations closer to the trailing edge ensures an adequate boundary layer thickness for the temperature sensors to capture multiple readings within the layer’s vertical span.

The corresponding local Reynolds numbers for these four locations are also provided in Table 2. All of these Reynolds numbers indicate predominantly laminar flow, as they are significantly lower than the early transition critical Reynolds number of 5×10^5 .

Table 2. Location data where thermal boundary layer thickness is measured experimentally.

Case Study	x_1 (cm)	x_2 (cm)	x_3 (cm)	x_4 (cm)	Re_{x1}	Re_{x2}	Re_{x3}	Re_{x4}
No-Inj-Tf50	43.20	40.10	37	33.90	11,045	10,253	9460	8668
No-Inj-Tf42	43.20	40.10	37	33.90	11,247	10,440	9633	8826

Re_{xi} are local Reynolds numbers.

Results of case studies No-Inj-Tf50 and No-Inj-Tf42 are displayed in Table 3 and Table 4, respectively.

Table 3. $T_a(y)$, y in cm, at designated stations for the case study of No-Inj-Tf50, $T_{\infty} = 29.38$ °C.

Station	$T_a(0)$ $U_{\infty} = 0.5$ m/s	$T_a(0.5)$ $U_{\infty} = 0.5$ m/s	$T_a(1)$ $U_{\infty} = 0.5$ m/s	$T_a(1.5)$ $U_{\infty} = 0.5$ m/s	$T_a(2)$ $U_{\infty} = 0.5$ m/s	$T_a(2.5)$ $U_{\infty} = 0.5$ m/s	$T_a(3)$ $U_{\infty} = 0.5$ m/s
x_1	71.50	46.06	34.88	31.42	30.61	29.36	29.36
x_2	71.50	45.73	34.63	31.20	30.30	29.36	29.36
x_3	71.50	45.27	34.28	30.89	30.01	29.36	29.36
x_4	71.50	44.82	33.94	30.58	29.70	29.36	29.36

Temperatures have an uncertainty of ± 0.10 °C.

Table 4. $T_a(y)$, y in cm, at designated stations for the case study of No-Inj-Tf42, $T_{\infty} = 30.09$ °C.

Station	$T_a(0)$ $U_{\infty} = 0.5$ m/s	$T_a(0.5)$ $U_{\infty} = 0.5$ m/s	$T_a(1)$ $U_{\infty} = 0.5$ m/s	$T_a(1.5)$ $U_{\infty} = 0.5$ m/s	$T_a(2)$ $U_{\infty} = 0.5$ m/s	$T_a(2.5)$ $U_{\infty} = 0.5$ m/s	$T_a(3)$ $U_{\infty} = 0.5$ m/s
x_1	55.50	42.17	34.17	31.90	30.44	30.07	30.07
x_2	55.50	41.75	33.93	31.88	30.24	30.07	30.07
x_3	55.50	41.33	33.59	31.30	30.16	30.07	30.07
x_4	55.50	40.92	33.26	30.96	30.10	30.07	30.07

Temperatures have an uncertainty of ± 0.10 °C.

Thermal boundary layer thickness $\delta_t(x)$ on a heated flat plate with a cold ambient is defined as the tranverse distance from the surface to such a point where $T_a \approx 1.01T_\infty$. In this contenxt, T_{a101} for the No-Inj-Tf50 case study is $1.01 \times 29.38 \text{ }^\circ\text{C} = 29.67 \text{ }^\circ\text{C}$, and similarly, for the case study of No-Inj-Tf42, $T_{a101} = 30.39 \text{ }^\circ\text{C}$. In order to find specific y at which T_{a101} is achieved for both cases, curve fitting is carried out using the Python programming language. This analysis is performed for each case study and for individual stations. An example Python script is provided in Appendix A for the station x_1 of the No-Inj-Tf50 case study.

The optimized curve fit for the case of No-Inj-Tf50 is shown in the Figure 5. The choice of fit function and the quality of the fit itself depend heavily on the number of data points in the dataset. A higher degree of fidelity in the curve fit generally requires around 8 to 10 data points. In this study, due to the limitations on the instrumentation at hand, the dataset is limited to six non-repeating values. Hence, the fit of the curve and fit function may not exhibit faithfulness. However, it is understood that the curve essentially becomes linear as temperatures approach T_∞ . Thus, assuming this linearity, the thermal boundary layer thickness $\delta_t(x)$ for all validation studies is provided in Table 5.

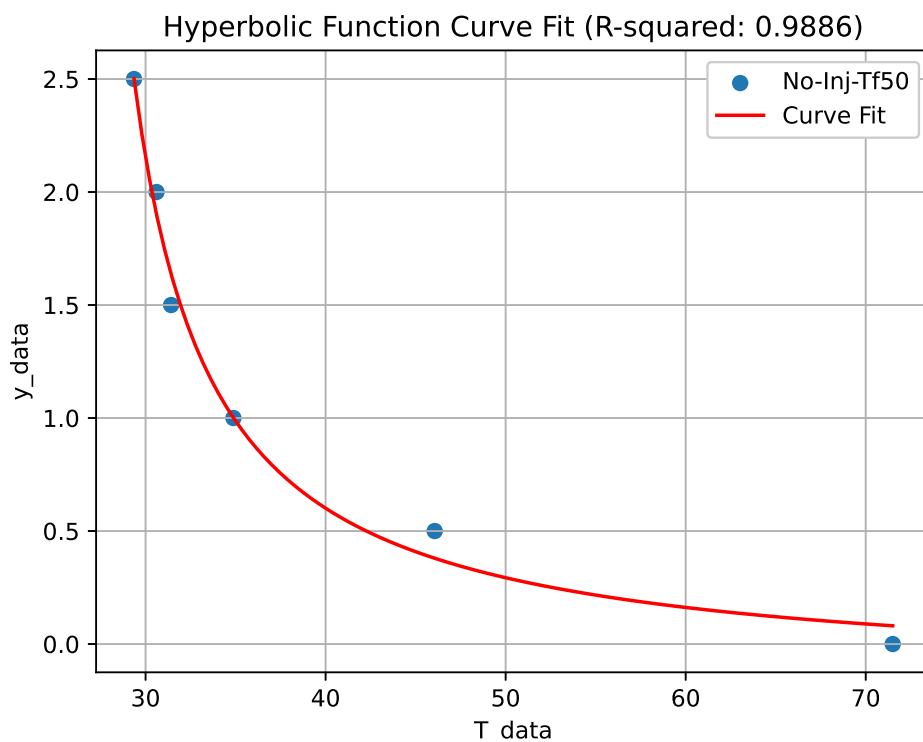


Figure 5. Hyperbolic curve fit to the No-Inj-Tf50 dataset.

Table 5. $\delta_t(x)$ for No-Inj-Tf50 and No-Inj-Tf42.

Case Study	δ_t at x_1 (cm)	δ_t at x_2 (cm)	δ_t at x_3 (cm)	δ_t at x_4 (cm)
No-Inj-Tf50	2.37	2.33	2.26	2.04
No-Inj-Tf42	2.07	1.95	1.92	1.83

Analytical thermal boundary layer relation is [28]

$$\delta_t = \frac{4.92x}{\sqrt[3]{Pr}\sqrt{Re_x}} \tag{1}$$

When comparing the samples of $\delta_t(x_1)$ for both No-Inj-Tf50 and No-Inj-Tf42, the authors observe that the absolute relative error in the estimation of δ_t at x_1 for No-Inj-Tf50

is 5.33%, and for No-Inj-Tf42, it is 7.17%. The errors are due to the idealized conditions assumed in Relation 1, whereas in a laboratory setup, achieving perfectly smooth laminar flow and completely lossless measurements is nearly impossible. Tables 6 and 7 compare the analytical and experimental thermal boundary layer thicknesses for the case studies of No-Inj-Tf50 and No-Inj-Tf42, respectively.

Table 6. $\delta_t(x)$ comparison for No-Inj-Tf50.

Stations	$\delta_t(x)$ Analytical Based on T_f	$\delta_t(x)$ Experimental	Relative Error %
x_1	2.28	2.37	3.95%
x_2	2.20	2.33	5.91%
x_3	2.11	2.26	7.11%
x_4	2.02	2.04	0.99%

Values are in cm.

Table 7. $\delta_t(x)$ comparison for No-Inj-Tf42.

Stations	$\delta_t(x)$ Analytical Based on T_f	$\delta_t(x)$ Experimental	Relative Error %
x_1	2.26	2.07	8.41%
x_2	2.18	1.95	10.55%
x_3	2.09	1.92	8.13%
x_4	2.01	1.83	9.00%

Values are in cm.

3.2. Thermal Boundary Layer Thickness over a Heated Flat Plate with Localized Cold Air Injections

In this study, four 3.5 mm holes were drilled into the flat plate at stations x_1 to x_4 . The experimental setup is detailed in Section 2. The results of case studies Inj-Tf45 and Inj-Tf39 are presented in Table 8 and Table 9, respectively, where $U_i = 0.3$ m/s is the injection flow speed, $T_i = 29.5$ °C is the fixed injection temperature.

Table 8. $T_a(y)$, y in cm, at designated stations for the case study of Inj-Tf45, $T_\infty = 32.50$ °C, $U_i = 0.3$ m/s, $T_p = 133.50$ °C, and $T_i = 29.5$ °C.

Station	$T_a(0)$ $U_\infty = 0.5$ m/s	$T_a(0.5)$ $U_\infty = 0.5$ m/s	$T_a(1)$ $U_\infty = 0.5$ m/s	$T_a(1.5)$ $U_\infty = 0.5$ m/s	$T_a(2)$ $U_\infty = 0.5$ m/s	$T_a(2.5)$ $U_\infty = 0.5$ m/s	$T_a(3)$ $U_\infty = 0.5$ m/s
x_1	58.76	47.75	38.50	35.25	33.76	32.80	32.49
x_2	58.76	43.15	37.65	34.50	33.25	32.49	32.49
x_3	58.76	39.35	36.45	33.55	33.03	32.49	32.49
x_4	58.76	35.51	35.35	33.04	32.90	32.49	32.49

Temperatures have an uncertainty of ± 0.15 °C.

Table 9. $T_a(y)$, y in cm, at designated stations for the case study of Inj-Tf39, $T_\infty = 32.50$ °C, $U_i = 0.3$ m/s, $T_p = 103.50$ °C, and $T_i = 29.5$ °C.

Station	$T_a(0)$ $U_\infty = 0.5$ m/s	$T_a(0.5)$ $U_\infty = 0.5$ m/s	$T_a(1)$ $U_\infty = 0.5$ m/s	$T_a(1.5)$ $U_\infty = 0.5$ m/s	$T_a(2)$ $U_\infty = 0.5$ m/s	$T_a(2.5)$ $U_\infty = 0.5$ m/s	$T_a(3)$ $U_\infty = 0.5$ m/s
x_1	55.50	43.85	37.59	35.34	33.57	32.67	32.49
x_2	55.50	39.64	36.78	34.31	33.13	32.49	32.49
x_3	55.50	36.84	35.98	33.31	32.91	32.49	32.49
x_4	55.50	34.40	33.20	32.98	32.58	32.49	32.49

Temperatures have an uncertainty of ± 0.15 °C.

The film temperatures T_f are calculated as the average of the first column (equilibrium surface temperatures when both U_i and U_∞ are active) and the ambient temperature of 32.50 Celsius. Therefore, T_f is 45.63 °C for Inj-Tf45 and 39.12 °C for Inj-Tf39. The thermal boundary layer thickness $\delta_t(x)$, for all experimental case studies is presented in Table 10.

Table 10. $\delta_t(x)$ in cm for Injection and No-Injection case studies.

Case Study	$\delta_t(x_1)$	$\delta_t(x_2)$	$\delta_t(x_3)$	$\delta_t(x_4)$
Inj-Tf45	2.51	2.26	2.17	2.06
Inj-Tf39	2.41	2.24	2.10	1.70
No-Inj-Tf50	2.37	2.33	2.26	2.04
No-Inj-Tf42	2.07	1.95	1.92	1.83

The film temperatures, T_f , in the injection study exhibit only slight differences from those observed in the validation study. Consequently, the analytical thermal boundary layer thickness in the injection study also remain the same up to two decimal places, as observed in the validation study. Tables 11 and 12 compare the analytical and experimental thermal boundary layer thickness for the case studies of Inj-Tf45 and Inj-Tf39, respectively.

It is important to note that these results were obtained after achieving thermal equilibrium. In order to ascertain thermal equilibrium, multiple sets of readings were taken at different time intervals awaiting steady states. However, despite these efforts, certain readings at station x_4 for Inj-Tf39 did not achieve steady states, most likely due to extended exposure of instrumentation and fittings to heat. Therefore, the authors choose to disregard the results from station x_4 as an isolated outlier.

Table 11. $\delta_t(x)$ comparison for Inj-Tf45.

Stations	$\delta_t(x)$ Analytical Based on T_f	$\delta_t(x)$ Experimental
x_1	2.28	2.51
x_2	2.20	2.26
x_3	2.11	2.17
x_4	2.02	2.06

Values are in cm.

Table 12. $\delta_t(x)$ comparison for Inj-Tf39.

Stations	$\delta_t(x)$ Analytical Based on T_f	$\delta_t(x)$ Experimental
x_1	2.26	2.41
x_2	2.18	2.24
x_3	2.09	2.10
x_4	2.01	1.70

Values are in cm.

4. Discussion and Conclusions

Authors argue that by focusing on a single variable (temperature), readers can gain a better and a more soft understanding of the possible underlying mechanisms at play. This is in contrast to the current literature, which often discusses multiple variables, sometimes obscuring the big picture. This study is a more nuanced approach directed at young researchers to try and scratch at the complexities inside the boundary layers especially when cold injections involve secondary motions. The existing laminar boundary layer theory finds thermal thickness based on the film temperatures assuming perfectly smooth laminar flow despite potential turbulent mixing inside the boundary layer due to cold transverse injections with the streamwise flow.

The results of this study suggest a general trend of increase in thermal boundary thickness due to cold air injections as evident from Tables 6, 7 and 10–12. The maximum enhancement is observed at x_1 for both case studies, Inj-Tf45 and Inj-Tf39. It is also observed that the higher the plate temperatures, the thicker the thermal boundary layer, especially at the trailing edge (x_1). The results are not unanimous and stereotypical as there are two results (Inj-Tf45 at $x_{2,3}$) which seem to suggest a slight decrease in thermal boundary layer thickness. This inconsistency could be attributed to measurement uncertainties and the

intricate physics both upstream and downstream, leading to instabilities. In contrast, the trailing edge station exhibits intriguing flow physics, primarily upstream.

In order to comprehend the possible rationale behind the observed trend of increase, readers must consider several complex mechanisms simultaneously. In the presence of a temperature difference, heat transfer occurs between the hot plate and the cold injected air. If the injected air does not mix well with the boundary layer, a layer of colder air can form above the boundary layer. This colder layer can act as an insulating layer, reducing the heat transfer from the plate to the fluid. As a result, the temperature gradient in the boundary layer may decrease, leading to an increase in the thermal boundary layer thickness. Cold air typically has a lower thermal diffusivity compared to the hot plate. Thermal diffusivity is a property that relates to the material's ability to conduct heat. As the injected cold air interacts with the boundary layer, its lower thermal diffusivity can decelerate the heat transfer process within the fluid, ultimately leading to a thicker thermal boundary layer.

Cold air injection can alter the properties of the fluid in the boundary layer. The reduced temperature due to the injection can cause changes in fluid viscosity and density. Changes in viscosity can affect the velocity profile, potentially leading to changes in the boundary layer thickness. Similarly, gradients in fluid density can influence the thermal boundary layer thickness by modifying the temperature and velocity gradients within the flow. Density gradients can also lead to vorticity and turbulence, thermal diffusivity gradients and varying convective heat transfer rates which can all affect the growth of the thermal boundary layer. The injection of cold air at a higher velocity than the incoming flow can disrupt the laminar flow and introduce turbulent flow characteristics. Turbulent flows typically exhibit thicker boundary layers than laminar flows, primarily due to heightened mixing and enhanced momentum and heat transfer. If the cold air injection induces turbulent flow or transition to turbulent flow, it can result in an increased thermal boundary layer thickness. It is important to note that the exact behavior of the thermal boundary layer in this scenario depends on various factors, such as the temperature difference between the injected air and the plate, the injection velocity, and the specific characteristics of the fluid and plate [29].

While conducting the experimental investigation, several limitations were encountered that may have influenced the study's outcomes. Firstly, due to the complexities of fluid dynamics and heat transfer phenomena, the laminar boundary layer's behavior can be highly sensitive to various factors, such as local variations in surface roughness or small changes in ambient conditions. Controlling these factors entirely during the experiments proved challenging and may have introduced uncertainties in the data. Additionally, the precise positioning of localized transverse cold air injections and the rate of injection were critical parameters that demanded precise calibration, but achieving perfect repeatability in practice was difficult. These experimental limitations necessitate caution when generalizing the results to different scenarios or flow conditions, emphasizing the need for further investigations and validation.

To enhance the robustness and applicability of the research findings, several recommendations are proposed for future studies in this area. Firstly, implementing advanced flow visualization techniques, such as Particle Image Velocimetry (PIV) or Laser Doppler Anemometry (LDA), can offer detailed insights into the boundary layer's velocity profiles and flow structures, complementing the temperature distribution data. Moreover, conducting a parametric study to investigate the influence of various geometric and flow parameters on the boundary layer's temperature distribution would provide a broader understanding of the system's behavior. Additionally, considering the transition from laminar to turbulent boundary layer regimes and studying the corresponding heat transfer characteristics could yield valuable comparisons and expand the research scope. Furthermore, integrating computational simulations, like Computational Fluid Dynamics (CFD), to validate the experimental results and gain insights into unmeasurable flow regions could enhance the accuracy of research and broaden its impact on engineering applications. Addressing these recommendations can foster a more comprehensive understanding

of the subject and produce more robust design and optimization strategies for practical engineering systems.

Author Contributions: Conceptualization, M.E.S. and A.A.M.; methodology, A.A.M.; software, F.S.B.; validation, F.S.B., M.E.S. and A.A.M.; formal analysis, F.S.B.; investigation, A.A.M.; resources, M.E.S.; data curation, A.A.M.; writing—original draft preparation, F.S.B.; writing—review and editing, A.A.M.; visualization, M.E.S.; supervision, A.A.M.; project administration, M.E.S.; funding acquisition, A.A.M. All authors have read and agreed to the published version of the manuscript.

Funding: This research work was funded by Institutional Fund Projects under grant no. (IFPIP: 1367-135-1443). The authors gratefully acknowledge technical and financial support provided by the Ministry of Education and King Abdulaziz University, DSR, Jeddah, Saudi Arabia.

Conflicts of Interest: The authors declare no conflict of interest. The funders had no role in the design of the study; in the collection, analyses, or interpretation of data; in the writing of the manuscript; or in the decision to publish the results.

Abbreviations

The following abbreviations are used in this manuscript:

RTD	Resistance Temperature Detectors
Pr	Prandtl number
Re	Reynolds number
Nu	Nusselt number
AC	Alternating Current
DC	Direct Current
PT	Platinum
RPM	Revolutions Per Minute

Appendix A. Python Script for Figure 5

```
import numpy as np
import matplotlib.pyplot as plt
from scipy.optimize import curve_fit
from sklearn.metrics import r2_score

# Define the hyperbolic function for curve fitting
def hyperbolic_function(T, a, b, c):
    return a + b / (T - c)

# Given data
y_data = np.array([0, 0.5, 1.0, 1.5, 2.0, 2.5])
T_data = np.array([71.5, 46.06, 34.88, 31.42, 30.61, 29.36])

# Perform the curve fit
params, _ = curve_fit(hyperbolic_function, T_data, y_data)

# Extract the optimized parameters
a_opt, b_opt, c_opt = params

# Generate points on the curve using the optimized parameters
T_curve = np.linspace(min(T_data), max(T_data), 100)
y_curve = hyperbolic_function(T_curve, a_opt, b_opt, c_opt)

# Calculate R-squared
y_predicted = hyperbolic_function(T_data, a_opt, b_opt, c_opt)
r2 = r2_score(y_data, y_predicted)
```

```

# Print the optimized parameters
print("Optimized Parameters:")
print("a =", a_opt)
print("b =", b_opt)
print("c =", c_opt)

# Print R-squared
print("R-squared:", r2)

# Plot the data points and the curve fit
plt.scatter(T_data, y_data, label='No-Inj-Tf50')
plt.plot(T_curve, y_curve, 'r-', label='Curve Fit')
plt.xlabel('T_data')
plt.ylabel('y_data')
plt.legend()
plt.title('Hyperbolic Function Curve Fit (R-squared: {:.4f})'.format(r2))
plt.grid(True)
plt.show()

```

References

1. Anderson, J.D. *Fundamentals of Aerodynamics*, 5th ed.; McGraw-Hill Education: New York, NY, USA, 2010.
2. White, F.M. *Viscous Fluid Flow*, 3rd ed.; McGraw-Hill Education: New York, NY, USA, 2006.
3. Schlichting, H.; Gersten, K. *Boundary-Layer Theory*, 9th ed.; Springer: Berlin, Germany, 2017.
4. Panton, R.L. *Incompressible Flow*, 4th ed.; Wiley: Hoboken, NJ, USA, 2012.
5. Lienhard, J.H. *A Heat Transfer Textbook*, 3rd ed.; Phlogiston Press: Cambridge, MA, USA, 2008.
6. Chedevergne, F.; Marchenay, Y. Transpired turbulent boundary layers: A general strategy for RANS turbulence models. *J. Turbul.* **2019**, *11–12*, 681–696. [\[CrossRef\]](#)
7. Ganic, E.N. Transpired boundary layers: A review. *Prog. Heat Mass Transf.* **1990**, *16*, 1–53.
8. Joshi, H.C. *Transpiration Cooling*; Cambridge University Press: Cambridge, UK, 2000.
9. Li, X.; Zhang, H. Transpired boundary layers: A review of recent progress. *Prog. Aerosp. Sci.* **2013**, *64*, 1–30.
10. Lachmann, G.V. (Ed.) *Boundary Layer Control, Vols. I and II*; Pergamon Press: New York, NY, USA, 1961.
11. Mickley, S.; Ross, R.C.; Squyers, A.C.; Stewart, W.E. *Heat, Mass and Momentum Transfer for Flow over a Flat Plate with Blowing or Suction*; NACA Technical Report TN-3208; NACA: Sacramento, CA, USA, 1955.
12. Brown, B.W.; Donoughe, P.L. *Tables of Exact Laminar Boundary Layer Solutions When the Wall Is Porous and Fluid Properties are Variable*; NACA Technical Report TN-2479; NACA: Sacramento, CA, USA, 1951.
13. Dorrance, W. *Viscous Hypersonic Flow*; McGraw-Hill Book Company, Inc.: New York, NY, USA, 1962.
14. Eckert, E.R.G.; Hayday, A.A.; Minkowycz, W.J. *Heat Transfer, Temperature Recovery, and Skin Friction on a Flat Plate Surface with Hydrogen Release into a Laminar Boundary Layer*; University of Minnesota Heat Transfer Laboratory Technical Report 27; University of Minnesota Heat Transfer Laboratory: St. Paul, MN, USA, 1961.
15. Sparrow, E.M.; Stan, J.B. The Transpiration Cooled Flat Plate with Various Thermal and Velocity Boundary Conditions. *Int. J. Heat Mass Transf.* **1966**, *9*, 508. [\[CrossRef\]](#)
16. Kubata, T.; Fernandez, F.L. Boundary Layer Flows with Large Injection and Heat Transfer. *AIAA J.* **1968**, *6*, 22–28. [\[CrossRef\]](#)
17. Gupta, P.S.; Gupta, A.S. Heat and mass transfer on a stretching sheet with suction or blowing. *Can. J. Chem. Eng.* **1977**, *55*, 744–746. [\[CrossRef\]](#)
18. Dutta, B.K.; Roy, P.; Gupta, A.S. Temperature field in flow over a stretching sheet with uniform heat flux. *Int. Commun. Heat Mass Transf.* **1985**, *12*, 89–94. [\[CrossRef\]](#)
19. Özisik, M.N. *Heat Transfer: A Basic Approach*; McGraw-Hill: New York, NY, USA, 1985.
20. Char, M.-I. Heat transfer of a continuous, stretching surface with suction or blowing. *J. Math. Anal. Appl.* **1988**, *135*, 568–580. [\[CrossRef\]](#)
21. Kays, W.M.; Crawford, M.E. *Convective Heat and Mass Transfer*; McGraw-Hill: New York, NY, USA, 1993.
22. Elhadidy, M.A.; Sabry, M. Experimental and numerical analysis of a solar air heater with transpired absorber. *Appl. Energy* **2009**, *86*, 1118–1127. [\[CrossRef\]](#)
23. Singh, R.; Saini, J.S. Performance evaluation of transpired solar collector: An experimental study. *Renew. Energy* **2013**, *60*, 586–592. [\[CrossRef\]](#)
24. Abdul-Aziz, A.R.; Sopian, K. A review on recent patents in transpired solar collector. *Recent Patents Mech. Eng.* **2015**, *8*, 203–214. [\[CrossRef\]](#)

25. Dong, H.; Zhao, X.; Li, Z.; Chen, Z. Experimental study on the effect of hole diameter on transpired solar collector performance. *Energy Procedia* **2016**, *88*, 37–42. [[CrossRef](#)]
26. Yuan, W.; Zhao, J.; Liu, W.; Du, J.; Zhang, Z. Experimental investigation on the thermal performance of the transpired solar collector with oblique v-groove. *Energy Convers. Manag.* **2017**, *135*, 153–160. [[CrossRef](#)]
27. Wu, X.; Song, B.; Li, Y.; Cai, Z.; Wang, R. Numerical simulation and optimization of heat transfer in transpired solar collector using the lattice Boltzmann method. *Energy Convers. Manag.* **2018**, *166*, 1–10. [[CrossRef](#)]
28. Forsberg, C.H. (Ed.) Chapter 6-Forced convection. In *Heat Transfer Principles and Applications*; Academic Press: Boca Raton, FL, USA, 2021; pp. 211–266; ISBN 978-0-12-802296-2. [[CrossRef](#)]
29. Tomić, M.A.; Ayed, S.K.; Stevanović, Ž.Ž.; Đekić, P.S.; Živković, P.M.; Vukić, M.V. Perforated plate convective heat transfer analysis. *Int. J. Therm. Sci.* **2018**, *124*, 300–306. [[CrossRef](#)]

Disclaimer/Publisher’s Note: The statements, opinions and data contained in all publications are solely those of the individual author(s) and contributor(s) and not of MDPI and/or the editor(s). MDPI and/or the editor(s) disclaim responsibility for any injury to people or property resulting from any ideas, methods, instructions or products referred to in the content.